Cement & Concrete Composites 34 (2012) 408–418

Contents lists available at SciVerse ScienceDirect

Cement & Concrete Composites

journal homepage: www.elsevier.com/locate/cemconcomp

Prediction of the diffusivity of cement-based materials using a three-dimensional spatial distribution model

Kiyofumi Kurumisawa [a,*], Toyoharu Nawa [a], Hitoshi Owada [b]

[a] Division of Sustainable Resources Engineering, Faculty of Engineering, Hokkaido University, Japan
[b] Radioactive Waste Management Funding and Research Center, 1-15-7 Tsukishima, Chuo-ku, Tokyo, Japan

ARTICLE INFO

Article history:
Received 4 February 2010
Received in revised form 18 November 2011
Accepted 21 November 2011
Available online 26 November 2011

Keywords:
Microstructure
Diffusion coefficient
Backscattered electron image
Image analysis
Micro-indentation

ABSTRACT

A three-dimensional image of hardened cement paste was reconstructed using a backscattered electron image (BEI) and used to predict the diffusion properties of hardened cement paste. After the BEI observations, an autocorrelation function (ACF) was calculated for each phase of the hardened cement paste, including the unhydrated cement, portlandite, and large pores. A three-dimensional image was reconstructed on the basis of the ACF based on random distributions. The dynamic elastic modulus and diffusion coefficient were calculated using a finite-element or finite difference method with the reconstructed three-dimensional images. The elastic modulus of the C–S–H phase was determined by micro-indentation, and the diffusivity of C–S–H was calculated using this elastic modulus based on previous reports. The resulting predicted dynamic elastic moduli and diffusion coefficients were in good agreement with the experimental results. Although, it was observed that the predicted values of the diffusivity of the blended cement pastes is different from the measured values, a new relationship between diffusivity and porosity of C–S–H in blended cement pastes was developed in this study.

1. Introduction

The durability of concrete strongly depends on its transport properties. Recently, the application of cement-based materials for the containment of low- and intermediate-level radioactive waste has generated considerable interest. In such applications it is important to be able to control the transport properties of the concrete, and also to be able to accurately predict the mass transport properties of concrete to ensure super long-term durability. Several models have been proposed for the prediction of mass transport properties of the concrete: Bentz proposed using a cement hydration reaction model [1], O'Neill Iqbal and Ishida developed a model based on thermodynamic principles [2], and Bejaoui and Bary predicted the diffusivity of concrete using an effective-medium theory [3]. However, the distribution and shape of pores and other hydrates in concrete was only considered in the model of Bentz [1]. Tanaka and Kurumisawa have determined the three-dimensional pore distribution using a gallium intrusion method with image analysis [4,5]. However, Kurumisawa et al. were unable to determine the distribution of unhydrated cement particles, calcium hydroxide, and other components of the concrete. Similarly, the effectiveness of pore structure evaluation by the image analysis is shown in previous report [6]. Models that can be used to determine the distribution of pores and a matrix using X-ray CT, microscopy, and other approaches, have been proposed in the field of geology [7–10]. For instance, a three-dimensional model of rocks has been reconstructed with autocorrelation functions using a two-dimensional section imaging system such as scanning electron microscopy. Although this model can be effectively applied to large pores e.g., pores with diameters of 100 μm, which are typical in rocks, it is difficult to apply this model to the pores of concrete because the size of concrete pores is much smaller, nano-scale.

In addition, concrete mixed with fly ash and blast furnace slag has become to be used widely recently to improve the durability of concrete structures, it is reported that the resulting microstructure is different from that of ordinary Portland cement alone. Therefore, it is necessary to establish the accurate microstructure for a precise evaluation, and for modeling.

This study attempted to reconstruct a three-dimensional image of hardened cement paste by considering autocorrelation functions measured using backscattered electron imaging. In particular, we focused on hardened cement paste because concrete properties depend on the properties of the hardened cement paste. Firstly, the validity of the reconstructed image model developed in this study was confirmed by a comparison of the measured and calculated dynamic elastic moduli of hardened cement pastes with a variety of water to cement ratios (W/C). Further, we predicted the diffusion

* Corresponding author. Tel./fax: +81 11 706 6319.
E-mail address: kurumi@eng.hokudai.ac.jp (K. Kurumisawa).

0958-9465/$ - see front matter © 2011 Elsevier Ltd. All rights reserved.
doi:10.1016/j.cemconcomp.2011.11.011

properties of hardened cement pastes and as well as blended cement pastes (fly ash and blast furnace slag) considering the nano-sized pores with the reconstructed image model. In order to detect the nano-sized pores, a micro-indentation method was used [11]. The resolution achieved with this method is lower than that of the nano-indentation method used by Ulm et al. [12,13], but the measurement employed here cover a similarly wide range of pore sizes.

By applying this method to existing concrete, it is possible to evaluate the properties of existing concrete structures from the microstructure level. Moreover, it will become possible to predict the diffusivity of blended cement pastes more accurately.

2. Experimental

2.1. Specimens

For the dynamic elastic modulus measurements, ordinary Portland cement (OPC) produced in Japan (Table 1) was used. The water/cement ratios used were 0.4, 0.6, 0.8, and 1.0 used to generate a variety of microstructures. The specimens were cast in 100 mm long and 50 mm diameter cylinders. The specimens were demolded after 24 h and cured in water at 20 °C for 28 days.

The diffusion measurements used cement pastes with water/cement (W/C) ratios of 0.3, 0.45, and 0.6 using OPC; fly ash cement pastes with replacement ratio 0.3 in each of the water to cement powder ratios (0.3, 0.45, 0.6), and slag cement paste with a replacement ratio 0.7 with the water to powder ratio 0.45. The physical properties and chemical compositions of the fly ash and slag are shown in Table 1[14]. The curing conditions were 1, 6, and 10 months in saturated calcium hydroxide water. The particulars of the specimens for diffusion measurement are listed in Table 2.

2.2. Backscattered electron image (BEI) measurement

A 5 mm cube was cut from a freeze-dried sample of the hardened cement pastes and used for the BEI observations. The freeze-dried specimens were immersed in epoxy resin in vacuum; after the epoxy resin hardened, the specimen surface was polished using SiC paper. Finally, the surfaces of the specimens were smoothed by 0.25 μm diamond paste, and a carbon coat was applied to provide electric conductivity on the specimen surface. The electron microscopy imaging was conducted under the following conditions: an acceleration voltage of 15 ke V, a working distance of 17 mm, an area size of 200 × 150 μm, and a pixel size of 0.32 μm. The resulting resolution in this study is 0.32 μm, and it was not possible to distinguish pores narrower than 0.32 μm in diameter. Observations were carried out on 16 fields in each specimen. Unhydrated cement (UH), unhydrated slag, calcium hydroxide (CH), C–S–H (including fine pores and other hydrates), fly ash, and pores larger than 0.32 μm were distinguished using image analysis software and setting brightness thresholds. The average area fraction of each phase was considered to be the volume fraction [15].

Table 2
Particulars of the specimens for diffusion measurement.

Symbol	W/B	Fly ash replacement ratio (%)	BFS replacement ratio (%)
O30	0.3	0	0
O45	0.45	0	0
O60	0.6	0	0
F30	0.3	30	0
F45	0.45	30	0
F60	0.6	30	0
B70	0.45	0	70

2.3. Pore structure measurements

The mercury intrusion method (MIP) and BET nitrogen adsorption were used for determining the pore structure. A 5 mm cubic sample was used for both MIP and BET.

2.4. Measurement of the microelastic modulus using a micro-indentation method

Specimens for indentation were the same as the specimens for BEI. Fichers scope (HC-100) was used for measuring the elastic modulus of the hydration products in the hardened cement paste, and 100 indents in a 10 × 10 μm grid were sampled in each specimen. The maximum load and speed were observed to be 20 mN and 1 mN/s, respectively. After the measurements, the indents were observed by microscopy to distinguish the different phases (UH, CH, C–S–H, and others).

2.5. Diffusion coefficient measurements

The diffusion cell method was used to measure the diffusion coefficients of 30 mm diameter 5 mm thick specimens. One side of the cell was filled by 0.5 mol/l NaCl solution and the other side with saturated $Ca(OH)_2$ solution. The concentration of Cl^- ions in the cell was established weekly by ion chromatography throughout the experiments. After reaching steady state conditions, the diffusion coefficient of a sample was determined by Eq. (1) with the slope of the time versus concentration plot,

$$D = \frac{L}{C_N}\left(\frac{dC}{dt}\cdot\frac{V}{A}\right) \quad (1)$$

where D, diffusion coefficient (m^2/s), L, thickness of specimen (m), A, area of specimen (m^2), V, volume of cell (m^3), C_N chloride ion concentration (mol/l), and dc/dt, gradient of concentration (mol/l/s). Two samples were used in the diffusion tests for each kind of specimen, and the average of the diffusion coefficients was adopted as the diffusivity.

2.6. Dynamic elastic modulus

The dynamic elastic modulus of solid components can be determined by testing the wave velocity with cylindrical specimens in a

Table 1
Physical properties and chemical compositions of the cementitious materials.

Material	Density (kg/m^3)	Blaine surface area (cm^2/g)	Chemical composition (%)					
			SiO_2	Al_2O_3	Fe_2O_3	CaO	MgO	SO_3
OPC	3170	3340	21.31	5.39	2.75	64.57	1.79	2.05
Fly ash	2260	3740	58.46	27.3	5.32	2.19	0.82	0.43
Slag	2880	4450	32.57	13.31	0.28	43.72	5.12	1.89

surface dry condition. The velocity in hardened cement paste is related both to the dynamic modulus E_d and to Poisson's ratio v. The dynamic elastic modulus E_d can be calculated by measuring V_p, the elastic wave velocity of the longitudinal wave (P wave), in the specimen [16]. The relationship between the physical properties and wave velocity V_p is given below:

$$E_d = V_p^2 \frac{\rho(1+v)(1-2v)}{1-v} \tag{2}$$

where ρ is the density of the specimen and v is Poisson's ratio (=0.25 in this study, because the effect of Poisson's ratio on the dynamic elastic modulus is not large.).

3. Modeling

3.1. Calculations for an autocorrelation function

To reconstruct a three-dimensional spatial image of the hardened cement paste, the autocorrelation function (ACF) was used for the different phases (UH, CH, pores, and other phases) to generate a binary image from the BEI without the C–S–H phase; the C–S–H phase was not included because it is the matrix and acts as a continuous phase in the hardened cement paste. The ACF is also known to be a two-point correlation function; it is defined as the probability that two arbitrary points are in the same phase as the function of the distance between them [17]. Therefore, the position of each phase can be determined using the ACF. The following procedure was used for calculating the ACF in this study [1]. The summation $S(x,y)$ was determined for an $M \times N$ image using the following equation:

$$S(x,y) = \sum_{i=1}^{M-x} \sum_{j=1}^{N-y} \frac{I(i,j) \times I(i+x, j+y)}{(M-x)(N-y)} \tag{3}$$

where $I(x,y)$ is 1 if the pixel at location (x,y) contains the phase(s) of interest, otherwise it is 0. $S(x,y)$ is then converted into the $S(r)$ function for the distance r in pixels using bilinear interpolation on the $S(x,y)$ values as follows:

$$S(r) = \frac{1}{2r+1} \sum_{l=0}^{2r} S\left(r, \frac{\pi l}{4r}\right) \tag{4}$$

3.2. Three-dimensional spatial image reconstruction

The ACF $S(r)$ for each phase mentioned above is used to reconstruct a three-dimensional image of the microstructure. The pixels in the three-dimensional spatial image is assigned random numbers with a normal distribution $N(x,y,z)$ that is generated using the Box–Muller method [1]. This random number distribution $N(x,y,z)$ is modified using the filter function $F(x,y,z)$ using the ACF $S(r)$. Finally, the resultant image $R(x,y,z)$ is generated using the following equation:

$$R(x,y,z) = \sum_{i=0}^{30} \sum_{j=0}^{30} \sum_{k=0}^{30} N(x+i, y+j, z+k) * F(i,j,k) \tag{5}$$

where $F(x,y,z)$ is determined using

$$F(r) = F(x,y,z) = \frac{\left[S\left(r = \sqrt{x^2+y^2+z^2}\right) - S(0) \times S(0)\right]}{[S(0) - S(0) \times S(0)]} \tag{6}$$

The threshold operation is carried out to obtain the appropriate volume fractions with respect to the pixels in $R(x,y,z)$ that were originally assigned to the respective phases of interest (UH, pores, or CH). For example, if a value of $R(x,y,z)$ is larger than the critical threshold, the pixel is assigned to the phase of interest; otherwise, it is assigned to the original phase. The reassigned number of pixels corresponds to the volume fraction measured using the BEI. The reconstructed size of the image is 100^3 voxels, with one voxel equivalent to $0.32\ \mu m^3$ according to the BEI observations. We reconstructed three different images with different random numbers to confirm the reproducibility of the model, and periodic conditions were also applied. For example, a three-dimensional image based on ACF and random distribution is shown in Fig. 1. Here two models with the same volume fraction of each phase have completely different microstructures, showing that ACF was an important factor in the generation of the spatial model.

3.3. Dynamic elastic modulus calculations using self-consistent analysis

The dynamic elastic modulus of the hardened cement paste was calculated by the self-consistent analysis (SCA) proposed by Oliver et al. [18]. The properties of composites such as hydrated cement pastes are determined by the SCA by applying the volume fraction and individual properties of each phase. The equations used in this study are given below:

$$E = \frac{9k\mu}{3k+\mu} \tag{7}$$

$$k = \sum_r f_r k_r \left(1 + \alpha\left(\frac{k_r}{k_0} - 1\right)\right)^{-1} \times \left[\sum_r f_r \left(1 + \alpha\left(\frac{k_r}{k_0} - 1\right)\right)^{-1}\right]^{-1} \tag{8}$$

$$\mu = \sum_r f_r \mu_r \left(1 + \beta\left(\frac{\mu_r}{\mu_0} - 1\right)\right)^{-1} \times \left[\sum_r f_r \left(1 + \beta\left(\frac{\mu_r}{\mu_0} - 1\right)\right)^{-1}\right]^{-1} \tag{9}$$

$$\alpha = \frac{3k_0}{3k_0 + 4\mu_0} \tag{10}$$

$$\beta = \frac{6(k_0 + 2\mu_0)}{5(3k_0 + 4\mu_0)} \tag{11}$$

where E is the dynamic elastic modulus (GPa); k, the bulk modulus (GPa); μ, the shear modulus (GPa); f, the volume fraction of each phase measured from the BEI; and the subscripts 0 and r denote the initial value and the phase, respectively. The input parameters for the bulk and shear moduli are listed in Table 3 [19]. The area fraction as measured from the BEI was used to determine the volume fraction of each phase.

3.4. Dynamic elastic modulus calculation using FEM

The reconstructed three-dimensional spatial images were input into the computer program elas3d.f, which was developed by Garboczi and Bohn [20,21]. This program treats each cubic voxel assigned to each phase as a trilinear finite element; the elastic equations are then discretized and solved by using a relaxation algorithm [22]. The dynamic elastic modulus was determined from the reconstructed three-dimensional spatial images with the periodic model of a microstructure using the relationship between the average stress and a given strain. The program has been successfully used for the calculation of the material properties of both hardened cement pastes and other compounds [23–27]. The bulk elastic modulus and shear elastic modulus of each phase used as the input in this study are listed in Table 3; they were the same as those used for the SCA calculations. In addition, the modulus of water was used for the pore spaces as they would be filled with water after the curing. The calculated size of FEM was the same as that obtained from the reconstructed image in 100^3 voxels.

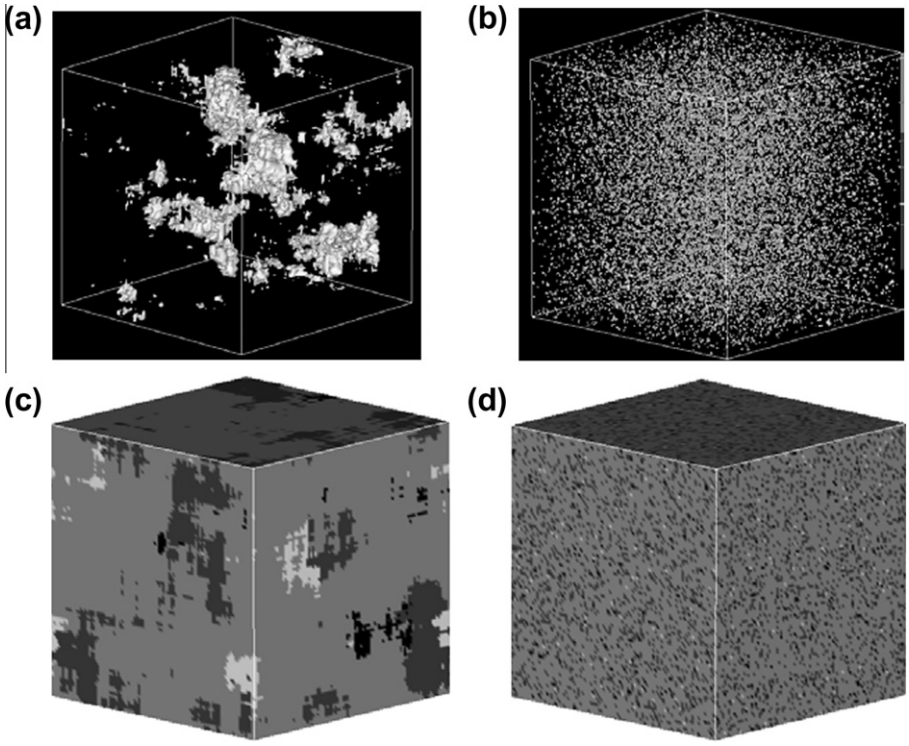

Fig. 1. Computed reconstructed three dimensional spatial distribution images: (a) pore distribution with ACF, (b) pore distribution with a random model, (c) phase distribution with ACF, and (d) phase distribution with random model (white: UH, dark gray: CH, light gray: C–S–H, black: Pores).

Table 3
Elastic modulus of the various phases [18].

Phase	Bulk elastic modulus (GPa)	Shear elastic modulus (GPa)
Unhydrated cement	105.2	44.8
Portlandite	40.0	16.0
C–S–H	14.9	9.0
Water	2.2	0.0

3.5. Predictions of diffusivity

The diffusivity in the reconstructed three-dimensional image is predicted on the basis of a model proposed by Garboczi and Bohn [20,21]. Garboczi proposed that the diffusivity in a steady state condition, as with conductivity, can be predicted by expressing it in the following Nernst–Einstein relation.

$$\frac{D}{D_0} = \frac{\sigma}{\sigma_0} \tag{12}$$

where D is the measured diffusivity; D_0, the diffusivity of the ions being considered in free water; σ_0, the conductivity of the solution in the pore space; and σ, the measured electrical conductivity. In addition, it is reported that the result obtained using the method proposed by Garboczi is the same as that obtained using a random walk method [28].

Because the diffusivity of chloride ions in the pores is known, the diffusivity of C–S–H can be estimated. For this calculation, firstly, the porosity of C–S–H can be calculated using the following equation, which is used in the packing model proposed by Jennings et al. [29].

$$P_{C-S-H} = 0.5 - 0.0077 \times E_{micro} \tag{13}$$

where P_{C-S-H} and E_{micro} are the porosity and elastic modulus, respectively, of the C–S–H phase. The elastic modulus can be determined by the micro-indentation method. The diffusivity of C–S–H was proposed by Bejaoui and Bary [3] to be a function of the C–S–H porosity (P_{C-S-H}) as shown it in Fig. 2. It was observed that high-density (HD)-C–S–H and low-density (LD)-C–S–H exhibited different diffusivities in that study:

$$D_{LD} = 1.34 * 10^{-10} * P_{C-S-H}^{2.09} \tag{14}$$

$$D_{HD} = 2.02 * 10^{-11} * P_{C-S-H}^{1.82} \tag{15}$$

where D_{LD} is the diffusivity of LD-C–S–H (m^2/s) and D_{HD} is the diffusivity of HD-C–S–H (m^2/s). The abovementioned porosity of C–S–H is calculated using the elastic modulus established with the micro-indentation method, and so the diffusivity of C–S–H can be also calculated. Finally, the capillary porosity was assigned a relative diffusivity of 1.0. The relative diffusivities of UH, CH, fly ash, and slag are all 0, and that of C–S–H is determined using the above expressions. In this study, the diffusivity of the C–S–H phase

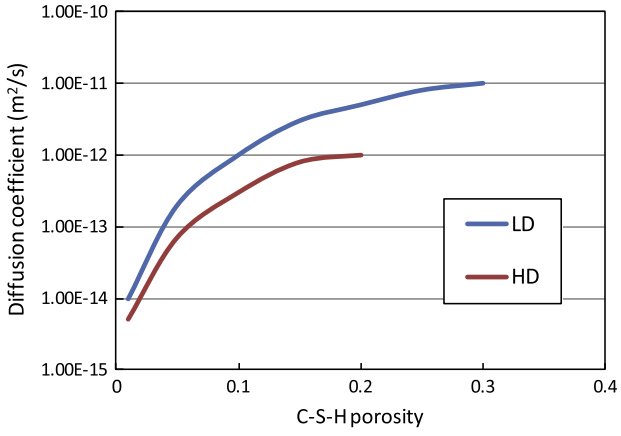

Fig. 2. Relationship between C–S–H porosities and diffusion coefficients [3].

of blended cement pastes is calculated from the relation of HD-C–S–H, because it is widely accepted that the diffusivity of blended cement is lower than that of OPC, and the diffusivity of chloride ions in the capillary pores was kept at 1.81×10^{-9} m^2/s [30].

4. Results and discussion

4.1. Validity of the reconstructed image model

4.1.1. Dynamic elastic modulus

The measured dynamic elastic moduli of the hardened cement pastes at 28 day are shown in Fig. 3. The dynamic elastic modulus decreased with *W*/*C* as would be generally expected.

4.1.2. BEI observations

Images of the BEI analysis obtained after 28 days are shown in Fig. 4. The black, dark gray, bright gray, and white portions in the BEI image correspond to pores, hydrated products, calcium hydroxide, and unhydrated cement, respectively. Only very few pores were visible in the specimen with a *W*/*C* of 0.4, but they are clearly present in the 0.6, 0.8, and 1.0 *W*/*C* specimens. The BEI cannot detect pores finer than the resolution limit of the microscope, as pointed out by Igarashi et al. [15]. Therefore, the porosity measured from the BEI would be lower than those determined with the results of different methods such as MIP. However, the quantity of unhydrated cement particles was approximately the same as that reported by Igarashi et al. [15]. The area fraction of each phase in the specimens as measured from the BEI is shown in Fig. 5. Porosity increased with increasing *W*/*C* ratio, but the quantity of unhydrated cement decreased.

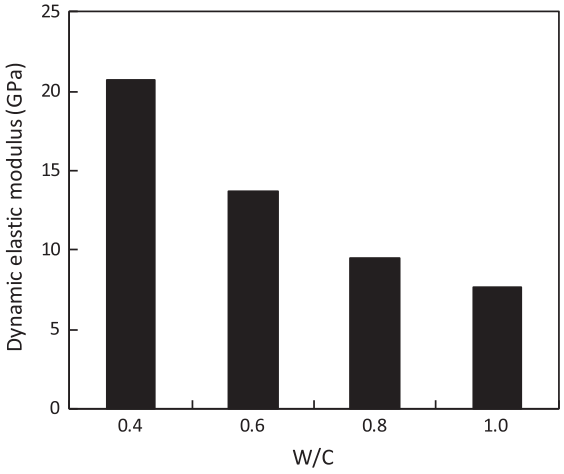

Fig. 3. Dynamic elastic modulus of hardened cement paste at 28 days for different *W*/*C* ratios.

4.1.3. Autocorrelation function

The ACF $S(r)$ in Eqs. (3) and (4) and the lineal path function $L(r)$ were calculated; the results are shown in Fig. 6. The value at distance 0 is equal to the fraction of the phase. At low *W*/*C* ratios, mostly unhydrated cement was present; for high *W*/*C* ratios there were many more pores. In different samples, different ACFs were observed, the ACF of CH, in particular, appeared to be the characteristic one. The production of calcium hydroxide may have differed with the *W*/*C* ratio, but the details are beyond the scope of this paper and are not discussed here. Each phase of the hardened cement paste may have been distributed at random because the ACF converged to the square of the value at distance 0. Therefore, the assumption that each phase was distributed at random may be considered through the reconstruction of the three-dimensional spatial model.

The maximum pore lengths in $L(r)$ were 20 and 2 μm for the *W*/*C* ratios of 1.0 and 0.4, respectively. A possible length scale reflecting the lineal continuity of each phase differed from the specimens, as shown by $L(r)$.

4.1.4. Microelastic modulus measurements by microindentation

The microelastic modulus of specimens after 28 days was measured by microindentations, and is shown in Fig. 7, median values for each specimen are shown in the figure. At the higher *W*/*C* ratios, the microelastic modulus was smaller because the quantity of pores in the contact area of the indentation affected the measured values. However, the microelastic moduli for the *W*/*C* ratios of 0.4 and 0.6 are very similar to those reported by Constantinides and Ulm [13].

4.1.5. Three-dimensional image reconstruction

Three-dimensional spatial images of hardened cement paste reconstructed using the method described in Section 3.2 above

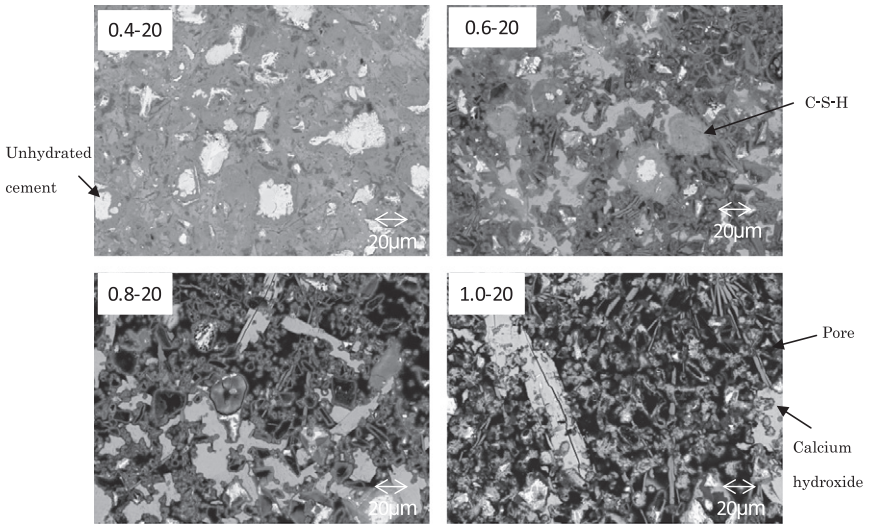

Fig. 4. Backscattered electron images of hardened cement paste at 28 days for different water–cement ratios (*W*/*C*s) (black: pore, dark grey: C–S–H, light grey: Calcium hydroxide, white: unhydrated cement).

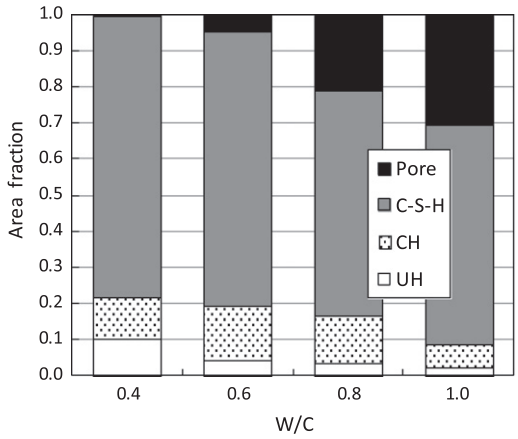

Fig. 5. Area fraction of the phases in hardened cement paste at 28 days. Pore: large capillary pores, C–S–H: Calcium Silicate Hydrate (including fine pores), UH: unhydrated cement particles, CH: calcium hydroxide crystals.

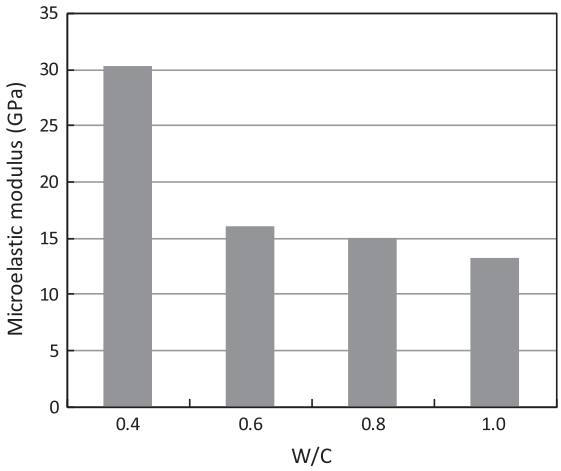

Fig. 7. Microelastic modulus values determined by microindentation.

are shown in Fig. 8. Black, dark gray, bright gray, and white denote the Pores, CH, C–S–H, and unhydrated cement phases, respectively, and it was thus possible to reconstruct three-dimensional image models for the different *W/C* specimens. The connectivity of the phases for the Pores, C–S–H, and Pore + C–S–H phases as calculated by Bentz's method [31] is shown in Fig. 9. The connectivity was zero when the phase volume fraction was less than 0.2, as also reported by Bentz and Garboczi [31]. We reconstructed three images of each specimen with different random numbers, but the connectivities were approximately the same. Thus it may be concluded that the dependence of the generated images on the used random numbers is negligible. The study here attempted the reconstruction of the three-dimensional images from the BEI using the ACF without the sintering algorithm for simplicity of the calculations [32].

4.1.6. Dynamic elastic modulus predictions using SCA and FEM

The relationship between the calculated dynamic elastic modulus using the SCA with values from Table 3 and the measured ones is shown in Fig. 10. There is an approximately linear relationship, but the value calculated using the SCA was higher than the measured ones, a reason for this may be because fine pores could not be detected by the BEI observations. The relationship between the dynamic elastic moduli calculated using the FEM and SCA is shown in Fig. 11, showing was a good correlation between the two. Overall, the three-dimensional image model proposed in this study is shown to perform the reconstruction adequately.

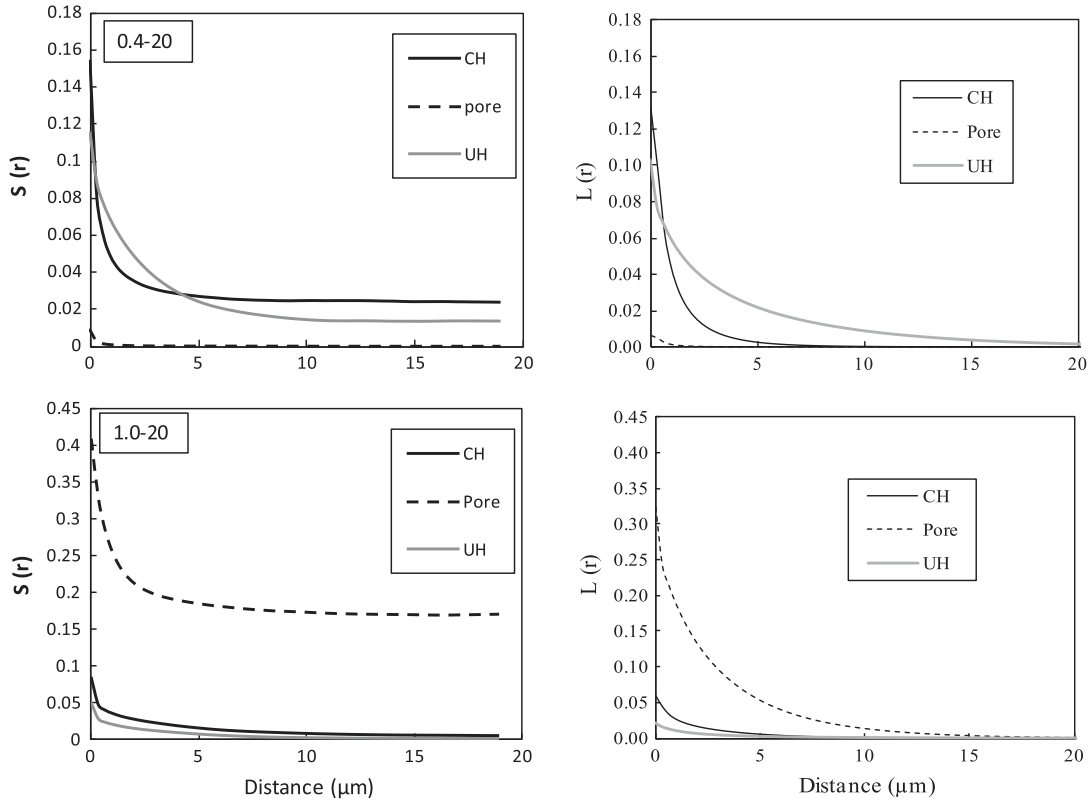

Fig. 6. Autocorrelation function and lineal path function for each phase in hardened cement paste at 28 days.

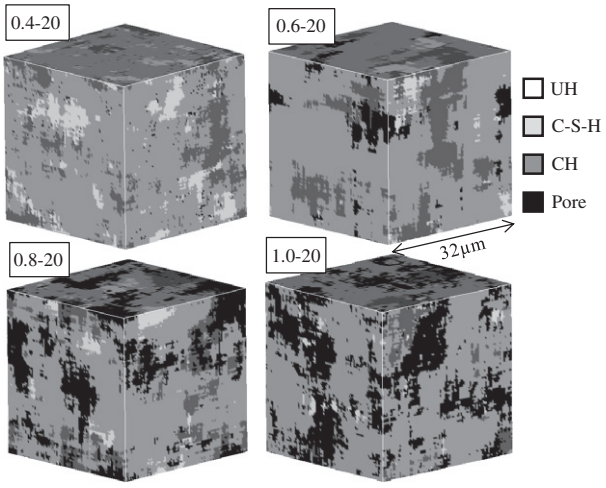

Fig. 8. Reconstructed three-dimensional images of hardened cement paste with different *W*/*C* ratios at 28 days.

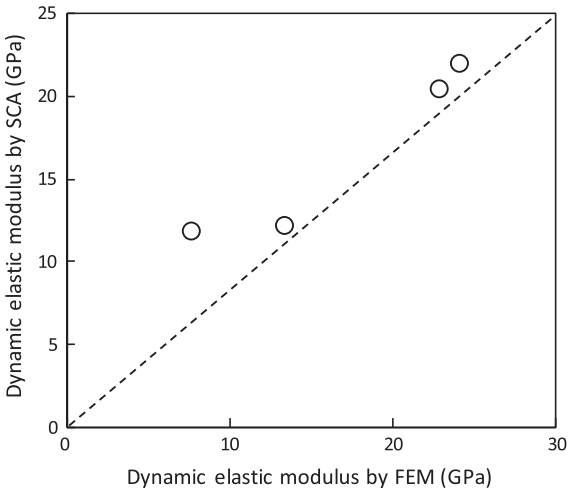

Fig. 11. Relationship between the dynamic elastic modulus predicted by SCA and FEM at 28 days.

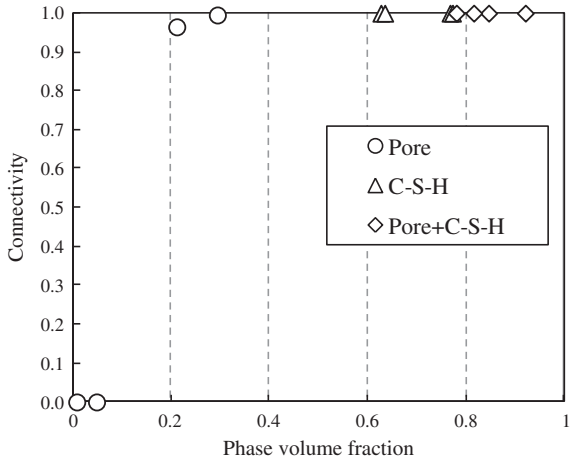

Fig. 9. Connectivity of phases for pores, C–S–H, and pores + C–S–H phases as calculated by the Bentz method.

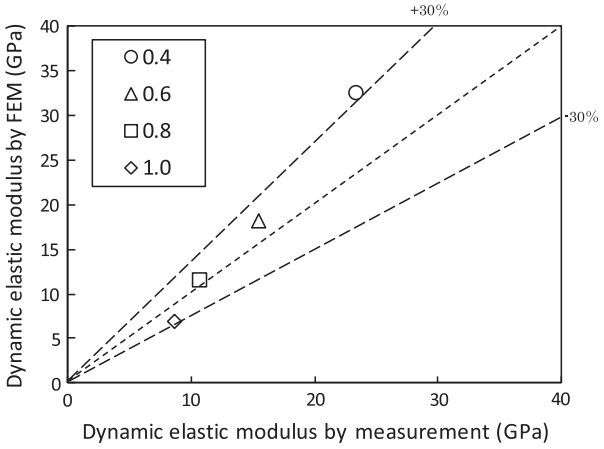

Fig. 12. Relationship between the dynamic elastic modulus as measured and predicted by FEM and modified by the C–S–H values determined by microindentation at 28 days.

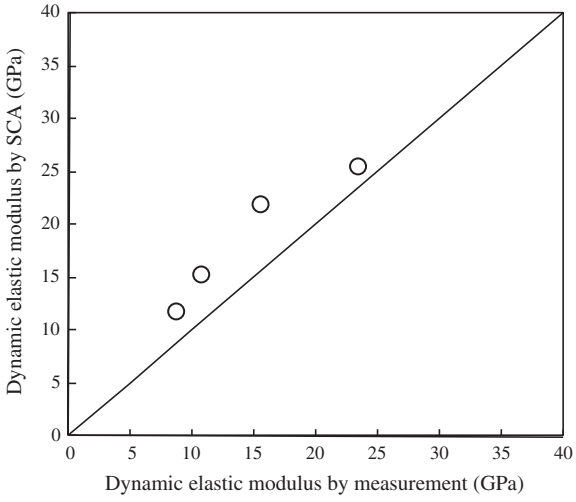

Fig. 10. Relationship between the dynamic elastic modulus as measured and predicted by the SCA at 28 days.

Next, we assumed that the elastic modulus of the C–S–H phase for the FEM calculation used the values provided by the microindentation (Fig. 7) because the detectable pore size in the BEI was more than 0.32 μm. The relationship between the calculated dynamic elastic modulus by FEM using the microindentation values and measurement results is plotted in Fig. 12. At lower *W*/*C* ratios, the dynamic elastic modulus calculated by FEM with the microindentation value was somewhat high because of the effect of the surrounding unhydrated cement on the C–S–H microelastic modulus. However, predicting the dynamic elastic modulus using the proposed three-dimensional image model was shown to be possible within an approximately 30% error. Therefore it would be appropriate for the elastic modulus of the C–S–H to use the value established with the micro-indentation method, leading to the conclusion that the porosity in the C–S–H phase can be measured by the micro-indentation method.

4.2. Prediction of diffusion coefficient

4.2.1. BEI results

Images of the BEI observations at 10 months are shown in Fig. 13. Unhydrated fly ash and slag are still remaining in these

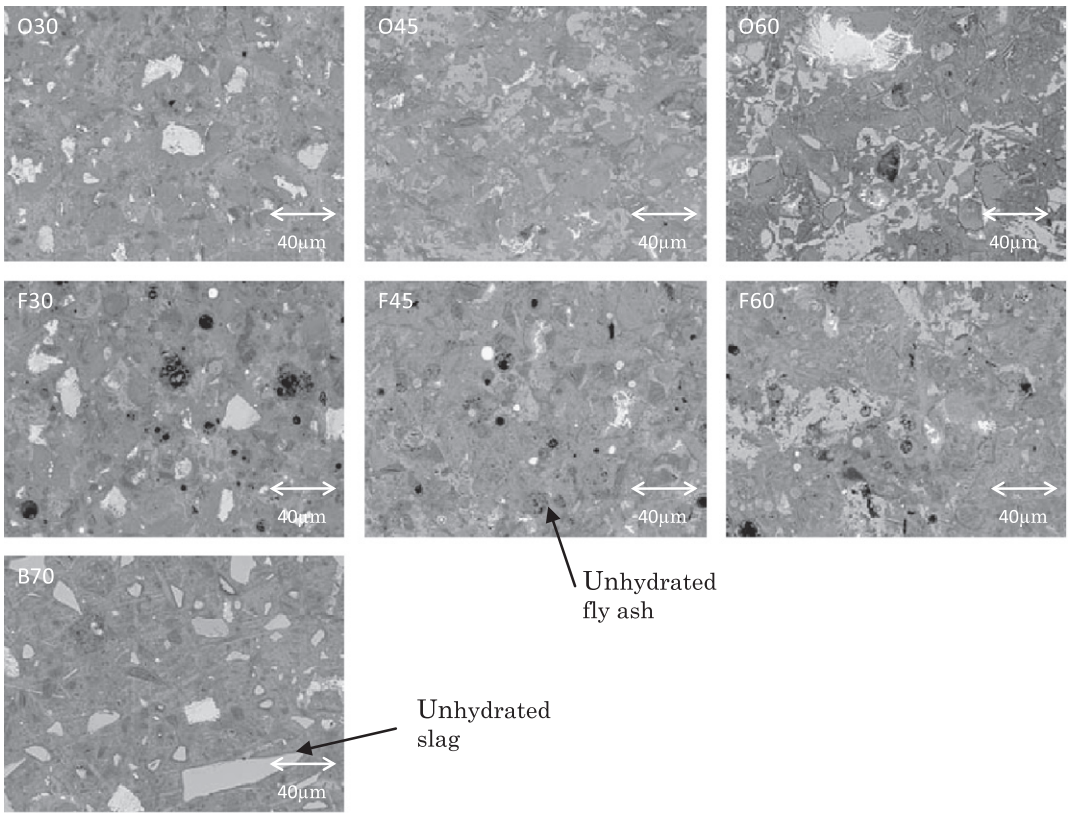

Fig. 13. BEI images of the specimens after 10 months curing.

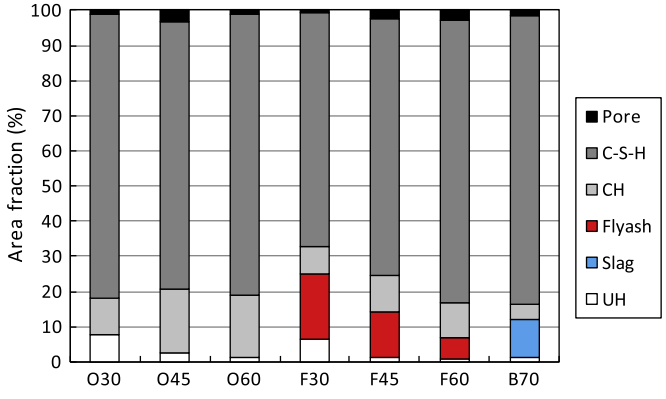

Fig. 14. Area fractions determined by BEI at 6 months curing.

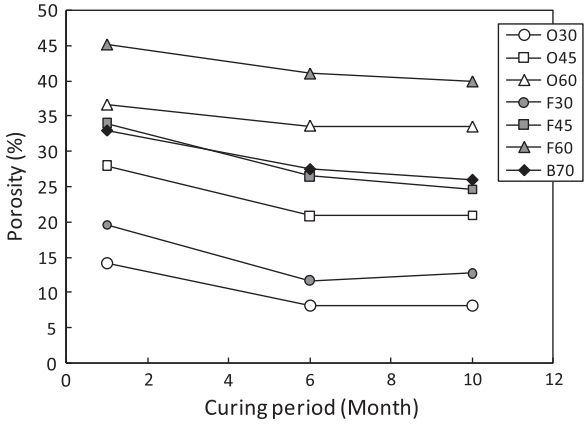

Fig. 15. Changes in porosities determined by MIP.

observations at 10 months. The results of the area fraction of each phase obtained from the BEI observations at 6 months are shown in Fig. 14. There is a large portion of C–S–H in every specimen, and there are very low percentages of large pores. However, Bentz reported that percolation occurred with more than 18% of pores [32]. This would lead to the surmise that the substances do not transport only through the large capillary pores. In addition, unhydrated fly ash and slag can still be observed in the blended cement pastes when observed at 6 months.

4.2.2. Pore structure

The changes in the porosity measured using MIP are shown in Fig. 15. The samples with low water-to-powder ratios showed low porosities, and the porosity decreased with increasing curing age. The porosity of the fly ash sample was higher than that of the OPC with the same water-to-powder ratio. The values of the porosities measured using the BET method are shown in Fig. 16. The porosities of F30 and F45 were all lower than those of O30 and O45, these results are different from those obtained using MIP; and the reasons behind this difference will need to be investigated.

4.2.3. Micro-indentation

The median values of the elastic modulus measured using the micro-indentation method for each specimen is shown in Fig. 17. Although the samples with low water-to-powder ratios exhibit higher elastic moduluses, the effect of the curing age on the elastic modulus is not completely clear. The range of elastic moduluses measured in this paper is intermediate between the LD-C–S–H

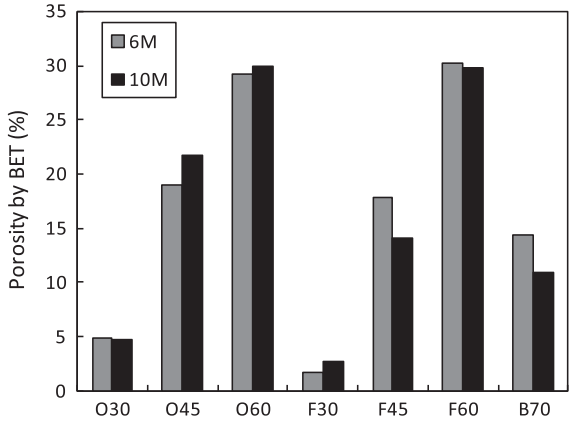

Fig. 16. Porosities determined by BET.

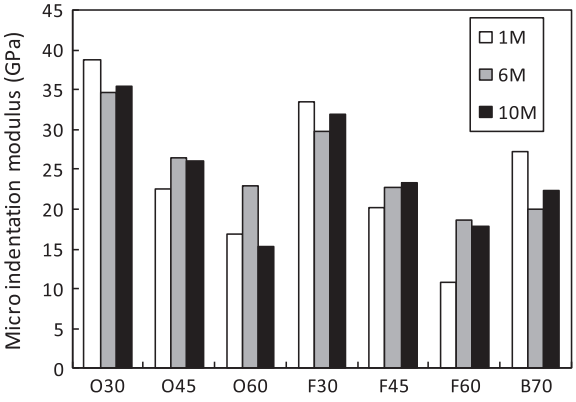

Fig. 17. Changes in micro elastic modulus with curing age.

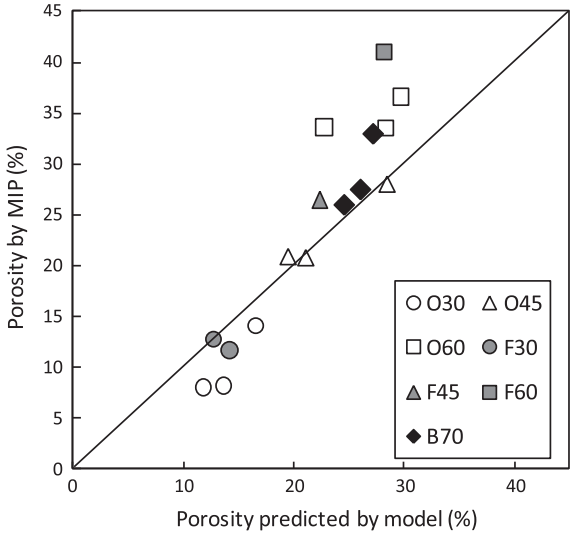

Fig. 18. Relationship between the experimentally determined and calculated porosities.

and the HD-C–S–H reported by Ulm [12,13].Fig. 18 shows the relationship of the porosity measured using MIP, and the sum of the porosity measured by BEI and the porosity of C–S–H calculated using Eq. (13). The measured and calculated porosities were approximately the same for all samples except for the samples with high water-to-powder ratios. Therefore, the assumptions

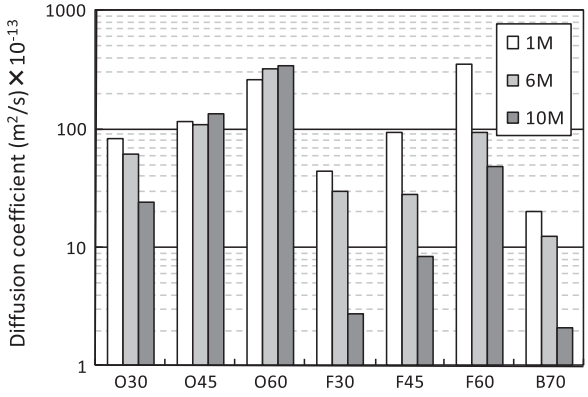

Fig. 19. Changes in diffusion coefficients with curing age.

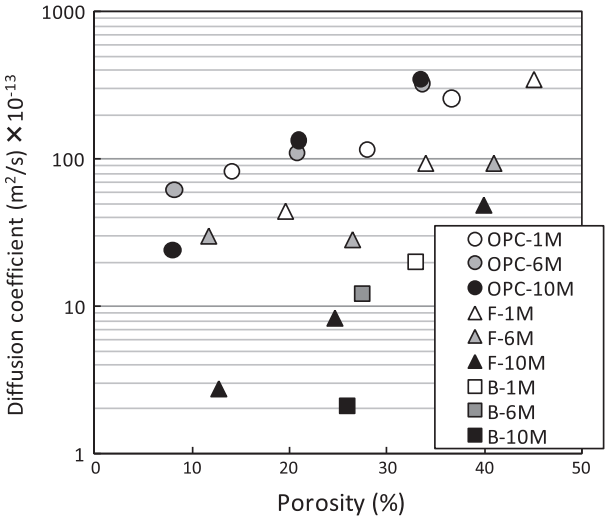

Fig. 20. Porosities determined by MIP plotted against the diffusion coefficients for different curing ages (OPC OPC paste, F: fly ash paste, B: slag paste, M: month(s)).

about the porosity made in this study may be concluded to be correct, that the microelastic modulus of C–S–H measured by microindentation includes the information of the small pores with less than 0.32 μm diameters.

4.2.4. Diffusion coefficient

The values of the measured diffusion coefficients are shown in Fig. 19. The diffusivity of the sample that contained fly ash and slag decreased with the progress of the curing, but that of the other samples did not change markedly. There was a large decrease in the diffusivity from 6 months to 10 months, particularly for the F30 and B70 samples. It is assumed that fly ash and slag underwent extensive reactions during this period; however, this is not discussed in further detail here because we did not measure the reaction ratios of these materials.

The effect of the porosity measured using MIP on the diffusivity is shown in Fig. 20. As mentioned in previous reports, the diffusivity increases with porosity. The diffusivity of the samples containing fly ash and slag was lower than that of OPC with the same porosity. It may be concluded that it is difficult to evaluate the diffusivity on the basis of porosity alone.

The relationship between the measured and predicted diffusivities based on Section 3.5 is shown in Fig. 21. The values of the predicted and measured diffusivities were approximately the same for all samples. Bentz et al. reported that the relative C–S–H diffusivity

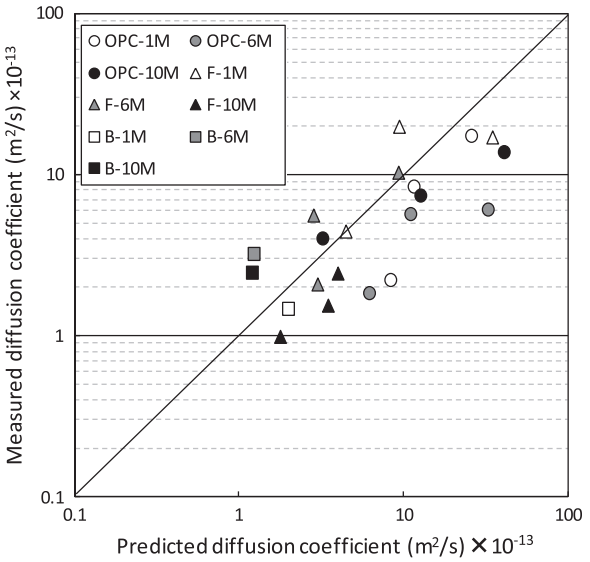

Fig. 21. Relationship between the measured and predicted diffusion coefficients (symbols as in Fig. 20).

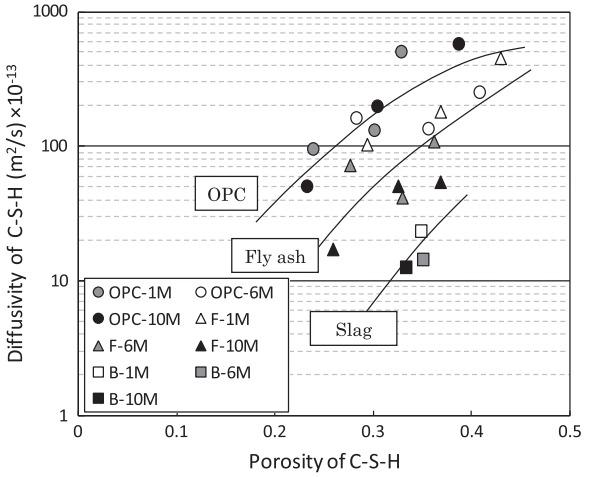

Fig. 22. Relationship between the calculated diffusivities and porosities of C–S–H by reverse analysis (symbols as in Fig. 20).

of OPC is 0.0025 and the pozzolanic C–S–H diffusivity is 0.0005 [33,34], the relative diffusivities used in this study range from 0.0001 to 0.014 calculated based on Section 3.5, that is, the value is very similar to that in the report of Bentz.

The diffusion coefficients of hardened cement paste in this report were predicted by using the relationship in a previous report above [3], and there was a small different result in all samples. To obtain an accurate relationship between the porosity and diffusivity of C–S–H, the diffusivity of C–S–H was calculated using reverse analysis on the basis of the experimental results, as shown in Fig. 22. The relationship between the diffusivity and porosity of C–S–H in OPC calculated by Eqs. (14) and (15) is different from that in the blended cement pastes, and the diffusivity of C–S–H produced by the pozzolanic reaction was 2–5 times smaller than that of OPC. Thus the relationship between diffusivity and porosity of C–S–H in OPC paste is different from that in blended cement pastes, this is because C–S–H is different for each of the blended cement pastes or because of an electric charge effect of the pore surface [35,36].

5. Conclusion

This paper developed a three-dimensional spatial distribution model on the basis of two-dimensional section images to predict the diffusion properties of hardened cement pastes. The validity of the reconstructed images was confirmed by a comparison of the measured and calculated dynamic elastic modulus with the microealstic modulus of C–S–H measured by a microindentation method. The measured value of the diffusivity was in good agreement with the value predicted for the diffusivity. This was established from the relationship between diffusivity and porosity of C–S–H determined by reverse analysis, which showed the relations for OPC paste, fly ash paste, slag paste were different. This difference possibly arises because of the very large differences between the pozzolanic C–S–H and OPC C–S–H or it may be because of the influence of the electric charge on the pore surface. Considering this, it may be concluded that C–S–H strongly influences the diffusion properties, and it will be necessary to establish the properties of C–S–H in more detail. However, in this study, it was still possible to predict the diffusivity of the hardened cement paste using fly ash and blast furnace slag by applying the relationship between the C–S–H porosity and diffusion coefficient, made possible by a reverse analysis.

Acknowledgments

This research include in a part of the results of "Evaluation Experiments of Long-Term Performance of Engineered Barriers" under a grant from the Japanese Ministry of Economy, Trade and Industry (METI), and Agency for Natural Resources and energy. We thank the Ministry of Education, Culture, Sports, Science and Technology for financial support with the research here.

References

[1] Bentz DP. CEMHYD3D: A Three-Dimensional Cement Hydration and Microstructure Development Modelling Package Version 2.0, NISTIR 6485; 2000.
[2] O'Neill Iqbal P, Ishida T. Modeling of chloride transport coupled with enhanced moisture conductivity in concrete exposed to marine environment. Cement Concrete Res 2009;39:329–39.
[3] Bejaoui S, Bary B. Modeling of the link between microstructure, effective diffusivity of cement pastes using a simplified composite model. Cement Concrete Res 2007;37:469–80.
[4] Tanaka K, Kurumisawa K. Development of technique for observing pores in hardened cement paste. Cement Concrete Res 2002;32(9):1435–41.
[5] Kurumisawa K, Tanaka K. Three-dimensional visualization of pore structure in hardened cement paste by the gallium intrusion technique. Cement Concrete Res 2006;36(2):330–6.
[6] Stroeven P, Hu J, Koleva DA. Concrete porosimetry: aspects of feasibility, reliability and economy. Cement Concrete Compos 2010;32(4):291–9.
[7] Liang ZR, Fernandes CP, Magnani FS, Philippi PC. A reconstruction technique for three-dimensional porous media using image analysis, Fourier transforms. J Petrol Sci Eng 1998;21:273–83.
[8] Adler PM, Jacquin CG, Quiblier JA. Flow in simulated porous media. Int J Multiphase Flow 1990;164:691–712.
[9] Quiblier JA. A new three-dimensional modeling technique for studying porous media. J Colloid Interface Sci 1984;98:84–102.
[10] Yao J, Frykman P, Kalaydjian F, Thovert JF, Adler PM. High-order moments of the phase function for real, reconstructed model porous media: a comparison. J Colloid Interface Sci 1993;156:478–90.
[11] Zhu W, Bartos PJM. Application of depth-sensing microindentation testing to study of interfacial transition zone in reinforced concrete. Cement Concrete Res 2000;30:299–304.
[12] Ulm F-J, Vandamme M, Bobko C, Ortega JA, Tai K, Ortiz C. Statistical indentation techniques for hydrated nanocomposites: concrete, bone, and shale. J Am Ceram Soc 2007;90(9):2677–92.
[13] Constantinides G, Ulm F-J. The effect of two types of C–S–H on the elasticity of cement-based materials: results from nanoindentation and micromechanical modeling. Cement Concrete Res 2004;34(1):67–80.
[14] H20 Report of Project for Evaluation on the long-term performance of engineered barrier system. Radioactive Waste Management Funding and Research Center; 2009.

[15] Igarashi S, Kawamura M, Watanabe A. Analysis of cement pastes, mortars by a combination of backscatter-based SEM image analysis, calculations based on the powers model. Cement Concrete Compos 2004;26:977–85.
[16] Zheng L, Sharon Huo X, Yuan Y. Experimental investigation on dynamic properties of rubberized concrete. Constr Build Mater 2008;22(5):939–47.
[17] Torquato S. Random heterogeneous materials: microstructure and macroscopic properties. Springer; 2001.
[18] Bernard O, Ulm F-J, Lemarchand E. A multiscale micromechanics-hydration model for the early-age elastic properties of cement-based materials. Cement Concrete Res 2003;33:1293–309.
[19] Haecker C-J, Garboczi EJ, Bullard JW, Bohn RB, Sun Z, Shah SP, et al. Modeling the linear elastic properties of Portland cement paste. Cement Concrete Res 2005;35:948–60.
[20] Garboczi EJ. Finite element and finite difference programs for computing the linear electric and elastic properties of digital images of random materials. National Institute of Standards and Technology, Internal Report 6269; 1998.
[21] Bohn RB, Garboczi EJ. User Manual for Finite Element and Finite Difference Programs: A Parallel Version of NIST IR 6269. NIST Internal Report 6997; 2003.
[22] Garboczi EJ, Day AR. An algorithm for computing the effective linear elastic properties of heterogeneous materials: three-dimensional results for composites with equal phase poisson ratios. J Mech Phys Solids 1995;43:1349–62.
[23] Roberts AP, Garboczi EJ. Elastic properties of a tungsten–silver composite by reconstruction and computation. J Mech Phys Solids 1999;47:2029–55.
[24] Roberts AP, Garboczi EJ. Elastic properties of model porous ceramics. J Am Ceram Soc 2003;83:3041–8.
[25] Meille S, Garboczi EJ. Linear elastic properties of 2-D and 3-D models of porous materials made from elongated objects. Mod Sim Mater Sci Eng 2001;9:1–20.
[26] Arns CH, Knackstedt MA, Pinczewski WV, Garboczi EJ. Computation of linear elastic properties from microtomographic images: methodology and agreement between theory and experiment. Geophysics 2002;67:396–1405.
[27] Kamali S, Moranville M, Garboczi E, Prené S, Gérard B. Influence of hydrate dissolution by water on the Young's modulus of cement-based materials. In: Proceedings of the 5th international conference on fracture mechanics of concrete and concrete structures; 2004. p. 631–8.
[28] Schwartz LM, Garboczi EJ, Bentz DP. Interfacial transport in porous media: application to DC electrical conductivity of mortars. J Appl Phys 1995;78:5898–908.
[29] Jennings HM et al. A multi-technique investigation of the nanoporosity of cement paste. Cement Concrete Res 2007;37(3):329–36.
[30] Mejlhede Jensen O, Freiesleben Hansen P, Coats AM, Glasser FP. Chloride ingress in cement paste and mortar. Cement Concrete Res 1999;29(9):497–504.
[31] Bentz DP, Garboczi EJ. Percolation of phases in a three-dimensional cement paste microstructural model. Cement Concrete Res 1991;21:325–44.
[32] Bentz DP, Martys NS. Hydraulic radius and transport in reconstructed model three-dimensional porous media. Transport Porous Media 1995;17:221–38.
[33] Garboczi EJ, Bentz DP. Computer simulation of the diffusivity of cement-based materials. J Mater Sci 1992;27:2083–92.
[34] Bentz DP, Jensen OM, Coats AM, Glasser FP. Influence of silica fume on diffusivity in cement-based materials I. Experimental and computer modeling studies on cement pastes. Cement Concrete Res 2000;30:953–62.
[35] Elakneswaran Y, Nawa T, Kurumisawa K. Influence of surface charge on ingress of chloride ion in hardened pastes. Mater Struct 2009;42:83–93.
[36] Elakneswaran Y, Iwasa A, Nawa T, Sato T, Kurumisawa K. Ion-cement hydrate interactions govern multi-ionic transport model for cementitious materials. Cement Concrete Res 2010;40:1756–65.